The immune response is a critical regulator of zebrafish retinal pigment epithelium regeneration

Lyndsay L. Leach[a,1], Nicholas J. Hanovice[a], Stephanie M. George[a], Ana E. Gabriel[a], and Jeffrey M. Gross[a,b,1]

[a]Department of Ophthalmology, University of Pittsburgh School of Medicine, Pittsburgh, PA 15213; and [b]Department of Developmental Biology, University of Pittsburgh School of Medicine, Pittsburgh, PA 15213

Edited by Sabine Fuhrmann, Vanderbilt University, Nashville, TN, and accepted by Editorial Board Member Jeremy Nathans April 16, 2021 (received for review August 21, 2020)

Loss of the retinal pigment epithelium (RPE) because of dysfunction or disease can lead to blindness in humans. Harnessing the intrinsic ability of the RPE to self-repair is an attractive therapeutic strategy; however, mammalian RPE is limited in its regenerative capacity. Zebrafish possess tremendous intrinsic regenerative potential in ocular tissues, including the RPE, but little is known about the mechanisms driving RPE regeneration. Here, utilizing transgenic and mutant zebrafish lines, pharmacological manipulations, transcriptomics, and imaging analyses, we identified elements of the immune response as critical mediators of intrinsic RPE regeneration. After genetic ablation, the RPE express immune-related genes, including leukocyte recruitment factors such as *interleukin 34*. We demonstrate that macrophage/microglia cells are responsive to RPE damage and that their function is required for the timely progression of the regenerative response. These data identify the molecular and cellular underpinnings of RPE regeneration and hold significant potential for translational approaches aimed toward promoting a pro-regenerative environment in mammalian RPE.

retinal pigment epithelium | regeneration | inflammation | macrophage | microglia

The retinal pigment epithelium (RPE) is a monolayer of polarized tissue spanning the posterior segment of the eye. Nestled between the light-sensing photoreceptors of the retina and the nutrient-delivering blood vessels of the choroid, the RPE serves as an intermediary between these tissues and comprises the blood–retinal barrier (BRB). As implicated by its location, the RPE performs myriad crucial functions to preserve the health of retinal and vascular tissues; furthermore, the RPE has a critical role in perpetuating the visual cycle and is integral to maintaining vision (1). Consequently, damage to the RPE compromises the functionality of the surrounding tissues and vision is severely impaired. Primary insult to the RPE occurs in ocular degenerative diseases, including the following: Stargardt disease (2); some forms of retinitis pigmentosa (3); and atrophic (or "dry") age-related macular degeneration (AMD) (4, 5), which is the more common form of AMD and a leading cause of blindness worldwide (6). There are currently no effective therapies for these RPE degenerative diseases. To compound the lack of treatment options, mammalian RPE and retinal tissues are limited in regenerative capacity, so tissue degeneration and consequent vision loss are irreversible. Gene therapy (7) and cell-replacement therapeutics (8, 9) are currently in clinical trials, but an attractive alternate treatment option lies in harnessing the intrinsic regenerative capacity of the RPE.

Vertebrate retinal regeneration has been extensively studied in both amniotes (e.g., birds and mammals) and anamniotes (e.g., fish and frogs) (10–12); however, little is known about the biology underlying RPE regeneration. Mammalian RPE can repair small lesions, but larger-scale restoration is not possible or leads to overproliferation and pathology (13). Some insight into the proliferative capacity of mammalian RPE has been gleaned from studies in mice (14, 15) and cultured human RPE (16), while studies in regeneration-capable nonmammalian systems have focused largely on RPE-to-retina transdifferentiation within the context of retinal regeneration (17). Thus, at present, the mechanisms driving intrinsic RPE regeneration remain elusive. Recently, we demonstrated the intrinsic capacity of zebrafish RPE to regenerate after widespread ablation, providing a model in which to study RPE regeneration (18).

Recent studies have converged on a role for immune-related systems during damage resolution in multiple model organisms and tissue contexts (19–26), including in the eye (27–32). Here, we identify the immune response as a critical mediator of zebrafish RPE regeneration in vivo. Our data show that immune-related genes are up-regulated in the RPE during early and peak stages of regeneration and that specific leukocytes respond to RPE ablation by infiltrating the injury site, proliferating, undergoing changes in morphology, and clearing tissue. RPE regeneration is impaired upon pharmacological dampening of inflammation, treatment with an inhibitor of macrophage colony stimulating factor 1 receptor (CSF-1R), and in an *irf8* mutant background, which is depleted of mature macrophages and lacks microglia at larval stages (33). Collectively, these results hold significant translational implications for mitigating RPE degenerative disease by revealing a role for the immune response in modulating the intrinsic ability of the RPE to regenerate.

Results

Immune-Related Gene Expression Signatures Are Up-Regulated in RPE during Regeneration. Utilizing a genetic ablation paradigm (*rpe65a*:nfsB-eGFP), we established that zebrafish can regenerate RPE (18); however, the signals involved in RPE regeneration remain unknown. In this

Significance

The retinal pigment epithelium (RPE) is an ocular tissue critical for maintaining a functional visual system, and death of RPE cells leads to blindness. Humans and other mammals are unable to regenerate the RPE, so vision loss is irreversible. Zebrafish are inherently capable of regenerating different types of tissues, including the RPE, and are therefore useful to understand and identify proregenerative pathways. Here, we show that elements of the immune response are critical for RPE regeneration. Knowledge gained using zebrafish can be applied to mammalian systems to try to stimulate RPE regeneration, with the overall goal of mitigating blinding disease in humans.

Author contributions: L.L.L., N.J.H., and J.M.G. designed research; L.L.L., S.M.G., and A.E.G. performed research; L.L.L. and J.M.G. contributed new reagents/analytic tools; L.L.L. analyzed data; and L.L.L. and J.M.G. wrote the paper.

Competing interest statement: L.L.L. is coinventor on US Patent #9,458,428, which is unrelated to the content herein.

This article is a PNAS Direct Submission. S.F. is a guest editor invited by the Editorial Board.

[1]To whom correspondence may be addressed. Email: lll42@pitt.edu or grossjm@pitt.edu.

This article contains supporting information online at https://www.pnas.org/lookup/suppl/doi:10.1073/pnas.2017198118/-/DCSupplemental.

Published May 18, 2021.

system, the RPE-specific (34) *rpe65a* enhancer drives expression of nitroreductase (nfsB) fused to eGFP. In the presence of nfsB, metronidazole (MTZ) is converted into an apoptosis-inducing agent that results in ablation of expressing cells (35). For all nfsB-MTZ ablation experiments, larvae were treated with 10 mM MTZ for 24 h, from 5 to 6 d after fertilization (dpf; i.e., 0 to 1 d after injury [dpi]), and subsequently allowed to recover. We utilized RNA-sequencing (RNA-seq) as an unbiased approach to identify RPE regenerative mechanisms. eGFP$^+$ RPE were isolated from dissociated enucleated eyes using fluorescence-activated cell sorting (FACS) at three time points: 2, 4, and 7 dpi with respective 7, 9, and 12 dpf age-matched controls (Fig. 1*A*). These time points were chosen as prior characterization identified early (2 dpi), peak (4 dpi), and late (7 dpi) stages of RPE regeneration discernible by resolution of apoptosis, peak proliferation, and recovery of RPE marker expression, respectively (18). To determine genes and pathways up-regulated during RPE regeneration, enriched Reactome pathways were identified from filtered differentially expressed genes (DEGs; Fig. 1 *B* and *C*). Innate/immune-response– and complement-related gene sets were enriched at 4 dpi (Fig. 1*C*), with various cytokines and cytokine receptors among the DEGs comprising these groups (*SI Appendix*, Table S2). Similarly, at 2 dpi, many cytokine genes (e.g., *il11b*, *il34*, *cxcl8a*, and *cxcl18b*) were up-regulated; in fact, *il11b* was the most highly up-regulated gene at this early regenerative time point (Fig. 1*D* and *SI Appendix*, Table S1). Analysis of RPE-specific markers revealed high expression in all eGFP$^+$ cell populations (*SI Appendix*, Fig. S1*A*; *columns 1*, *3*, *5*, and *7*) and low to no expression of neutrophil or macrophage and microglia markers (*SI Appendix*, Fig. S1*B*; *columns 1*, *3*, *5*, and *7*). An exception was the 4 dpi MTZ+ RPE dataset (*SI Appendix*, Fig. S1; *column 7*), which showed enrichment of several macrophage and microglia

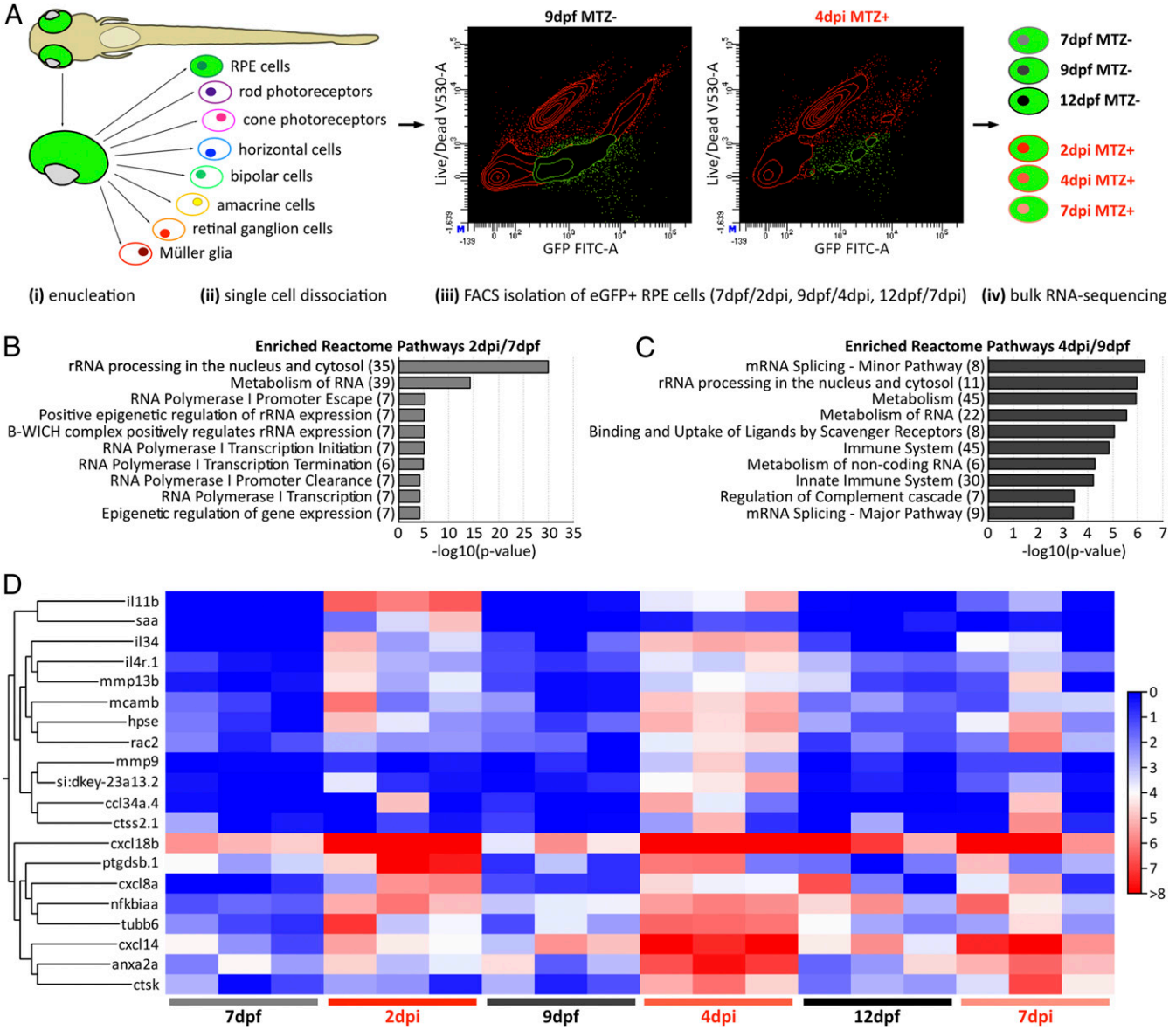

Fig. 1. Enrichment of immune system genes during RPE regeneration. (*A*) Experimental workflow showing steps for tissue processing (*i*, *ii*) and isolation of eGFP$^+$ RPE (*iii*, *iv*). Example 9 dpf and 4 dpi FACS plots showing cell sorting gate (*iii*; green). (*B* and *C*) Top Reactome pathways enriched from groups of significant DEGs at 2 dpi/7 dpf (*B*) and 4 dpi/9 dpf (*C*). Numbers in parentheses indicate quantities of significantly enriched DEGs. (*D*) Heatmap showing hierarchical clustering of immune-related genes in the top 50 up-regulated DEG sets from 2 dpi/7 dpf and 4 dpi/9 dpf (*SI Appendix*, Tables S1 and S2). Heatmap legend represents $\log_2$ (transcripts per million +1).

markers (e.g., *apoeb, irf8*, *lcp1*, *mfap4*, and *mpeg1.1*). This is possibly due to phagocytosis of $eGFP^+$ debris by these leukocytes after ablation (see below) (25, 26, 31). Despite this, 4 dpi RPE RNA-seq samples showed high expression of *il11b*, *il34*, and *cxcl18b* when qualitatively compared with 4 dpi macrophage and microglia RNA-seq samples (*SI Appendix*, Fig. S1*C*; *columns 7* and *8*). Leukocyte recruitment factors, *il34*, *cxcl8a*, and *cxcl18b*, were among the top-50 up-regulated DEGs in RPE at both 2 dpi and 4 dpi (*SI Appendix*, Tables S1 and S2). Interleukin-34 (IL-34) is a known ligand for CSF-1R (36) and an important signal for recruitment, proliferation, and differentiation of macrophages and microglia (37, 38), while Cxcl8 and Cxcl18b are potent neutrophil recruitment factors (39, 40). Differential expression of *il34*, *cxcl8a*, and *cxcl18b* was not significantly up-regulated at 7 dpi (*SI Appendix*, Table S3), suggesting that leukocytes are no longer recruited at this stage. Lists of top down-regulated DEGs can be found in *SI Appendix*, Tables S4–S6. Previous literature highlights a role for immune function in an ocular regenerative context (29–32), and these data indicate that immune-related genes, which include those encoding critical mediators of leukocyte recruitment and function, are also up-regulated during RPE regeneration.

Macrophages/Microglia Respond After RPE Ablation at Key Regenerative Timepoints. Next, we wanted to understand the temporal dynamics of leukocyte infiltration between the time spanning RPE ablation and peak regeneration. Zebrafish do not develop adaptive immunity until at least 3 wk after fertilization (41), so only innate immune cells (neutrophils and macrophages) were examined. Neutrophil infiltration was assessed using the transgenic reporter line *lyz:*TagRFP (42). In the majority of unablated larvae, there were no *lyz:*$TagRFP^+$ cells observed in the RPE in whole-mount eyes from 6 to 9 dpf (Fig. 2 *A–D*). In ablated larvae, few *lyz:*$TagRFP^+$ cells were apparent in the RPE from 1 to 4 dpi (Fig. 2 *E–H*). *lyz:*-$TagRFP^+$ cells mobilized to the eye after ventral needle poke, indicating neutrophils are responsive to ocular injury (*SI Appendix*, Fig. S2). *lyz:*$TagRFP^+$ cell number quantification showed no significant difference in infiltration at 1, 3, or 4 dpi but a significant increase at 2 dpi when compared with 7 dpf controls (Fig. 2*Q*). However, six neutrophils was the maximum observed in the RPE of any larva, and this was only in one larva from the 2 dpi dataset (Fig. 2 *F* and *Q*).

To assess macrophage infiltration dynamics, a 4C4 antibody (Fig. 2 *I–P* and *R*; ref. 43) and the transgenic reporter line *mpeg1:*mCherry (*SI Appendix*, Fig. S3; ref. 44) were used for visualization. Notably, neither method distinguishes monocyte-derived macrophages from tissue resident macrophage (or microglia) populations and the 4C4 antigen is not known, so cells will be referred to collectively as macrophages/microglia (MΦs/μglia) hereafter. Resident $4C4^+$ and $mCherry^+$ MΦs/μglia were present in the RPE of unablated larvae in whole-mount (Fig. 2 *I–L*) and sectioned tissue (*SI Appendix*, Fig. S3). From 2 to 4 dpi, ablated larvae showed an increase in 4C4 (Fig. 2 *N–P*) and mCherry signal (*SI Appendix*, Fig. S3). Due to clustering of both $4C4^+$ and $mCherry^+$ cells, percent area quantification was performed as individual cells were difficult to distinguish for counting (e.g., Fig. 2*O*). 4C4 quantification revealed a significant increase from 2 to 4 dpi, with peak infiltration occurring at 3 dpi (Fig. 2 *O* and *R*). Similarly, mCherry significantly increased from 2 to 4 dpi and peaked at 3 dpi (*SI Appendix*, Fig. S3 *K*, *L*, and *Q*). Importantly, MTZ treatment alone did not mobilize MΦs/μglia to the RPE, as an influx of $mCherry^+$ cells was not observed in 4 dpi larvae lacking the *rpe65a:*nfsB-eGFP transgene (*SI Appendix*, Fig. S3*R*).

In addition to MΦ/μglia influx after RPE ablation, we also noted phenotypic differences in $4C4^+$ cells (Fig. 2 *I–P*, *Insets*). Macrophages and microglia are morphologically dynamic cells at rest and in response to injury and disease. This process is complex and controversial, but an overly simplified summary is that ramified cells retract cellular extensions and become rounded (amoeboid) after injury, which may signify phagocytic function (45). $4C4^+$ cells in unablated larvae appeared ramified (Fig. 2 *I–L*, *Insets*), while $4C4^+$ cells in ablated larvae appeared more amoeboid, which was most obvious at the 2 to 4 dpi time points (Fig. 2 *M–P*, *Insets*). Accordingly, we assessed cell morphology in vivo from 2 to 4 dpi, the times when MΦs/μglia infiltrate the RPE, using light-sheet microscopy and the transgenic reporter line *mpeg1.1:*Dendra2 (46). Dendra2 is a fluorescent photoconvertible protein that irreversibly switches green to red when exposed to violet or ultraviolet (UV) light (47); here, conversions were performed immediately prior to imaging for all larvae. We utilized Imaris to three-dimensional (3D) render, isosurface, and quantify the sphericity (48) of anterior *mpeg1.1:*$Dendra2\ (red)^+$ cells in larvae from 2 to 4 dpi (Fig. 3 and *SI Appendix*, Fig. S4 and Movies S1–S6). At 3 dpi, but not 2 dpi and 4 dpi (*SI Appendix*, Fig. S4 *C* and *F*), ablated larvae had *mpeg1.1:*$Dendra2\ (red)^+$ cells that were significantly more spherical, when compared with 8 dpf unablated siblings (Fig. 3*C*). Consistent with previous findings after central nervous system (CNS) injury in zebrafish (25, 26, 31), these data suggest that MΦs/μglia may be phagocytic in response to RPE injury during the time of peak infiltration. Indeed, examination of sectioned tissue at 3 dpi revealed a tight association between $mCherry^+$ cells and $eGFP^+$ debris, supporting active phagocytosis by MΦs/μglia (Fig. 3 *D–G*).

To directly assess MΦ/μglia gene expression during RPE regeneration, we utilized *mpeg1:*mCherry zebrafish (44) and performed RNA-seq analyses on FACS-isolated $mCherry^+$ MΦs/μglia (*SI Appendix*, Fig. S5 *A–D*). Early-(2 dpi) and peak-(4 dpi) regeneration stages were selected to align with the RPE RNA-seq time points; however, we chose to forego analysis at 7 dpi as there were few DEGs in RPE at this time point (*SI Appendix*, Tables S3 and S6) and MΦ/μglia infiltration appeared to wane after 3 dpi (Fig. 2*R* and *SI Appendix*, Fig. S3*Q*). Isolation of MΦs/μglia was confirmed using expression of *apoeb*, *csf1ra/b*, *grn1*, *irf8*, *lcp1*, *mfap4*, and *mpeg1.1* (*SI Appendix*, Fig. S1*B*; *columns 2*, *4*, *6*, and *8*). Neutrophil (*SI Appendix*, Fig. S1*B*) and RPE (*SI Appendix*, Fig. S1*A*) marker expression was low or absent in the MΦ/μglia datasets. Pathway analysis of significant up-regulated DEGs showed that cell cycle– and mitosis-related Reactome gene sets were among the top 10 highly enriched pathways in MΦs/μglia at 2 and 4 dpi (Fig. 4 *A* and *B*). Full lists of enriched Reactome pathways can be found in *SI Appendix*, Tables S9 and S10. Genes within the top-enriched Reactome Cell Cycle, Mitotic pathway were also found to be among the top 50 most significantly up-regulated DEGs at both time points, and these included *cdk1*, cyclins, cell division cycle, and cytokinesis genes, among others (Fig. 4*C* and *SI Appendix*, Tables S7 and S8). Macrophage populations proliferate in response to injury, inflammatory, and other disease stimuli (49), and in zebrafish, cell cycle genes are up-regulated in microglia after CNS injury (26). We have shown that isolated RPE express *il34*, a known proproliferative factor for macrophage and microglia cells (38), at 2 and 4 dpi (Fig. 1*D*), suggesting that MΦs/μglia may proliferate in response to RPE-derived cytokine stimulus. To assess this, larvae were pulsed with EdU for 2 h at 2 and 4 dpi and fixed. EdU colabeling with $mCherry^+$ cells was observed in the RPE and retina (Fig. 4 *D–G*), and there were significantly more EdU^+ $mCherry^+$ cells in these tissues at 2 dpi (Fig. 4 *H* and *I*). Additionally, annexin A1, *anxa1a*, was significantly up-regulated at 2 dpi (*SI Appendix*, Table S7). AnxA1 has been associated with macrophage phagocytosis (50, 51), and *anxa1a* is expressed at the same time that $4C4^+$ cells appear rounded (2 dpi; Fig. 2*N*). These findings combined with colocalization of $mCherry^+$ cells and RPE debris at 3 dpi (Fig. 3 *D–G*) and the presence of MΦ/μglia markers in RPE datasets at 4 dpi (*SI Appendix*, Fig. S1*B*) indicate that infiltrating MΦs/μglia may be functioning to internalize debris within the injury site.

Collectively, these data show that MΦs/μglia respond during RPE regeneration as these cells appeared to infiltrate the RPE injury site, take on a more amoeboid morphology, and proliferate

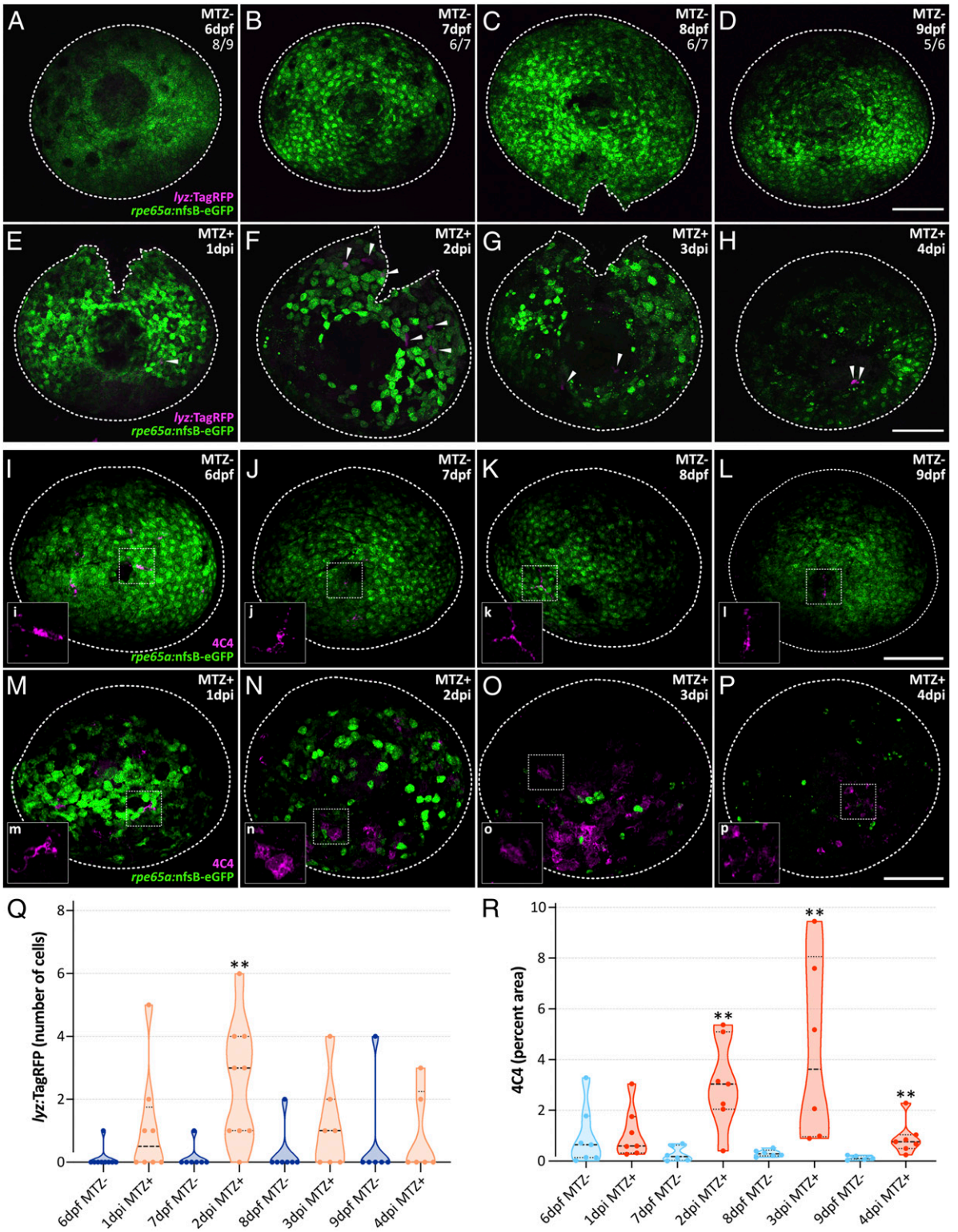

Fig. 2. Leukocyte infiltration into the RPE injury site during regeneration. (*A–H*) Confocal micrographs of MTZ− (*A–D*) and MTZ+ (*E–H*) Tg(*lyz*:TagRFP;*rpe65a*:nfsB-eGFP) whole-mount eyes. Ratios at top right (*A–D*) indicate number of eyes lacking *lyz*:TagRFP^{+} neutrophils (white arrowheads in *E–H* over total number of eyes). (*I–P*) Fluorescent confocal micrographs of MTZ− (*I–L*) and MTZ+ (*M–P*) Tg(*rpe65a*:nfsB-eGFP) whole-mount eyes labeled with 4C4 to mark MΦs/μglia. (*I–P*) *Insets* show digital zooms of single cells or cell clusters to highlight 4C4^{+} cell morphologies. (*A–P*) White dashed lines designate edges of eyes. Magenta labels endogenous TagRFP or 4C4 and green labels endogenous eGFP. (Scale bars, 100 μm.) (*Q*) Violin plots showing a significant increase in the number of *lyz*:TagRFP^{+} neutrophils at 2 dpi when compared with 7 dpf controls. A maximum of six infiltrating cells were present at 2 dpi (datapoint in *F*). (*R*) Violin plots showing significant increases in 4C4^{+} staining from 2 to 4 dpi (MTZ+) when compared with MTZ− controls. (*Q* and *R*) Dashed black lines represent the median, and dotted black lines represent quartiles. *SI Appendix*, Table S12 contains statistical information. Dorsal is up; ***P* value ≤0.01.

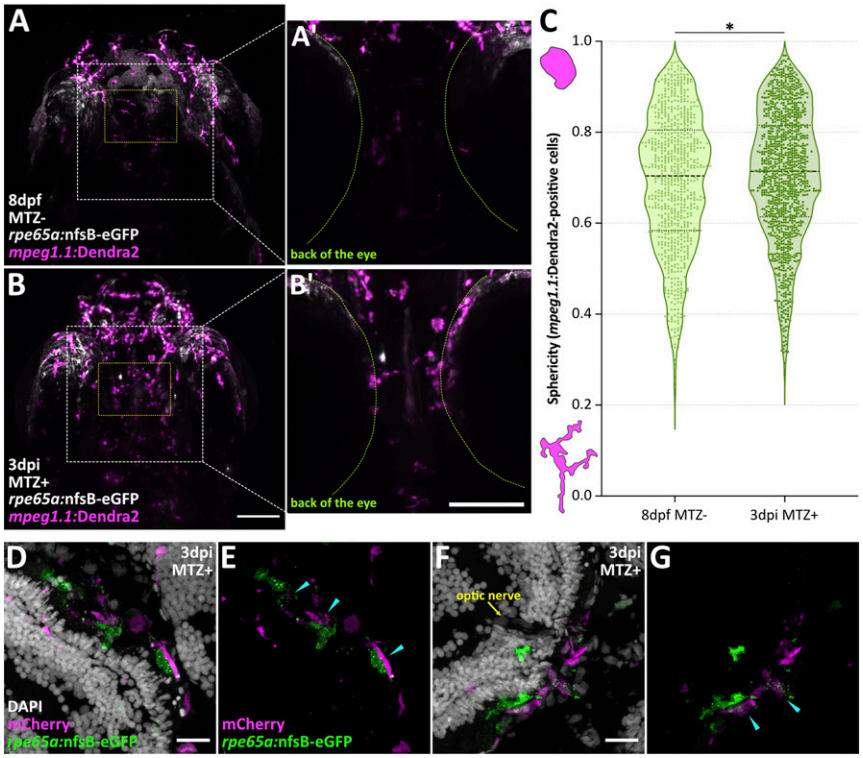

Fig. 3. Macrophages/microglia show increased sphericity and association with RPE debris at 3 dpi. In vivo light-sheet micrographs from 8 dpf MTZ– (*A* and *A′*) and 3 dpi MTZ+ (*B* and *B′*) Tg(*mpeg1.1*:-Dendra2;*rpe65a*:nfsB-eGFP) larvae. (*A′* and *B′*) Digital zooms of cropped 100 μm z-stacks (z-step = 100 to 200) showing *mpeg1.1*:Dendra2 (red)$^+$ cell localization (magenta) in/adjacent to the back of the eye (green dashed line). (*A* and *B′*) White labels endogenous eGFP. Yellow boxes correspond to areas shown in Movies S2 and S3 (*A*) and in Movies S5 and S6 (*B*). Anterior is up. (Scale bars, 100 μm.) (*C*) Violin plots showing a significant increase in sphericity of anterior *mpeg1.1*:Dendra2 (red)$^+$ cells in 3 dpi MTZ+ larvae when compared with 8 dpf MTZ– controls. *SI Appendix*, Table S12 contains statistical information. Dashed black lines represent the median, and dotted black lines represent quartiles; **P* value ≤ 0.05. (*D–G*) Confocal micrographs of transverse sections from 3 dpi MTZ+ Tg(*mpeg1*:mCherry; *rpe65a*:nfsB-eGFP) larval eyes. Cyan arrowheads point to MΦs/μglia (magenta) overlapping with RPE debris (green) in central–dorsal (*D* and *E*) and central–ventral (*F* and *G*) regions. Dorsal is up; anterior is left. (Scale bars, 20 μm.)

at time points when *il34* (a proproliferative signal) is significantly up-regulated in regenerating RPE. MΦs/μglia play dual roles in both promoting and resolving inflammation and are capable of switching from pro- to anti-inflammatory phenotypes to restore damaged tissue (52); thus, these findings prompted us to more closely investigate inflammation, and MΦs/μglia specifically, as critical mediators of RPE regeneration.

Pharmacological Inhibition of Inflammation Impairs RPE Regeneration. Inflammatory responses are critical for CNS regeneration in zebrafish (24, 29, 32), so we wanted to determine if broadly dampening inflammation attenuated RPE regeneration. Larvae were exposed to 50 μM dexamethasone, a synthetic glucocorticoid (GC) and potent anti-inflammatory agent, or 0.05% dimethyl sulfoxide (DMSO) for 24 h prior to RPE ablation, for the 24-h duration of ablation with MTZ, and for the entirety of the regeneration period, which was taken out to 4 dpi (Fig. 5*A*). Efficacy of systemic dexamethasone treatment was confirmed by quantifying expression of *pxr*, a transcriptional target of dexamethasone (53), which was up-regulated after 24-h dexamethasone exposure (Fig. 5*B*). Previously, proliferation and pigment recovery, measured based on central expansion of continuous pigmented tissue (*SI Appendix*, Fig. S6*A*), were quantified as metrics of RPE regeneration after ablation (18), and other studies have used a similar approach (24, 29, 32). As proliferation peaks between 3 to 4 dpi and visible pigment is largely recovered in regenerating RPE by 4 dpi (18), we used the same methodology here. Proliferation was assayed by treating larvae with 10 mM BrdU for 24 h, from 3 to 4 dpi (Fig. 5*A*). Results showed significantly fewer RPE-localized BrdU$^+$ cells (Fig. 5 *C*, *E* and *G*) and a significant decrease in pigment recovery (Fig. 5 *D*, *F*, and *H*) in dexamethasone-treated 4 dpi larvae when compared with 4 dpi DMSO-treated siblings. Dexamethasone treatment showed no effect on cell proliferation in 9 dpf unablated siblings (*SI Appendix*, Fig. S6 *B–D*). To determine if dexamethasone impaired MΦ/μglia recruitment, larvae were stained with 4C4 at 8 dpf/3 dpi (peak MΦ/μglia infiltration; Fig. 2). As anticipated, there were few 4C4$^+$ cells in 8 dpf unablated controls (*SI Appendix*, Fig. S7 *A* and *B*) and abundant 4C4$^+$ signal in 3 dpi ablated DMSO controls (*SI Appendix*, Fig. S7*C*). Interestingly, 4C4 also labeled dexamethasone-treated 3 dpi ablated larvae (*SI Appendix*, Fig. S7*D*), and there was no significant difference in 4C4$^+$ area between these larvae and DMSO-treated controls (*SI Appendix*, Fig. S7*E*). Together, these data indicate that inflammation is necessary for RPE regeneration, but dexamethasone treatment does not impact recruitment of leukocytes after ablation.

Macrophage/Microglia Function Is Required for RPE Regeneration. Next, we wanted to determine if MΦs/μglia are required for RPE regeneration and utilized two independent perturbations to manipulate MΦ/μglia function: an *irf8* mutant zebrafish line (33) and a pharmacological inhibitor of CSF-1R, PLX3397. Irf8 is an important regulator of monocyte/macrophage (54) and microglia (55) lineages. *irf8* mutant zebrafish are devoid of microglia to 31 dpf and lack macrophages during the early stages of larval development, which begin to recover (but remain small and immature) by 7 dpf (33). We found 4C4$^+$ cells were present in *irf8* wild-type and mutant ablated larvae at 4 dpi (*SI Appendix*, Fig. S8 *A–E*); however, average cell size was smaller in *irf8* mutants (*SI Appendix*, Fig. S8*F*), consistent with previous reports that *irf8* mutant macrophages may be immature despite recovery (33). As noted above, *irf8* was enriched in 4 dpi RPE RNA-seq samples, possibly stemming from phagocytic MΦ/μglia collection (*SI Appendix*, Fig. S1*B*). It is also possible that *irf8* plays a direct role in the RPE; however, *irf8* mutant RPE appeared mature and morphologically normal at 6 dpf (*SI Appendix*, Fig. S9 *A–F*) and relative *irf8* expression levels analyzed by qRT-PCR, while showing an upward trend at 4 dpi, were low overall comparative to *rpe65a* (*SI Appendix*, Fig. S9*G*). With this caveat in mind, we also utilized PLX3397, previously shown to deplete macrophages and microglia (56–58) and/or impair polarization (58, 59), to independently assess MΦ/μglia function during RPE regeneration. Using a treatment regimen identical to dexamethasone (Fig. 5*A*), *mpeg1*:mCherry$^+$ signal depletion was observed in unablated (*SI Appendix*, Fig. S8

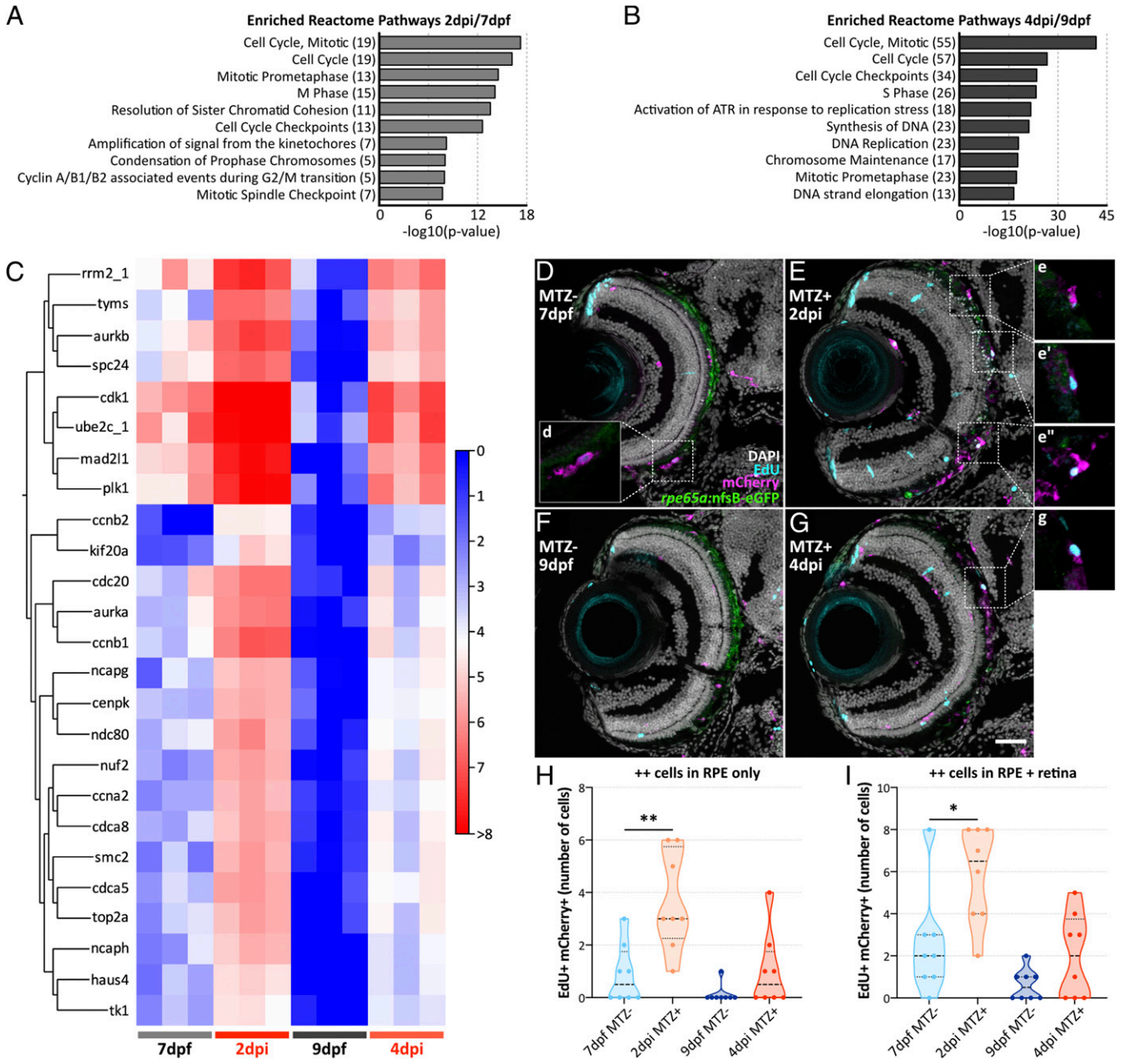

Fig. 4. Proliferation signatures are present in macrophages/microglia during RPE regeneration. Top 10 Reactome pathways enriched from groups of significantly up-regulated DEGs at 2 dpi/7 dpf (*A*) and 4 dpi/9 dpf (*B*) in FACS-isolated mCherry$^+$ MΦs/μglia. Numbers in parentheses indicate quantities of significantly enriched DEGs. (*C*) Heatmap showing hierarchical clustering of cell cycle– and mitosis-related genes selected for representation based on presence in the top 50 up-regulated gene sets from 2 dpi/7 dpf and 4 dpi/9 dpf DEG analyses (*SI Appendix*, Tables S7 and S8). Heatmap legend represents $\log_2$ (transcripts per million +1). Confocal micrographs of transverse sections from MTZ– and MTZ+ Tg(*mpeg1*:mCherry; *rpe65a*:nfsB-eGFP) eyes at 7 dpf/2 dpi (*D* and *E*) and 9 dpf/4 dpi (*F* and *G*). Digital zooms (*D*–*E″* and *G*) highlight proliferating (EdU$^+$; cyan) mCherry$^+$ MΦs/μglia (magenta). (Scale bar, 40 μm.) (*H* and *I*) Violin plots showing significant increases in EdU$^+$ mCherry$^+$ costaining in the RPE (*H*) and in the RPE and retina (*I*) of 2 dpi MTZ+ larvae. Dashed black lines represent the median, and dotted black lines represent quartiles. *SI Appendix*, Table S12 contains statistical information. Dorsal is up; **P* value ≤ 0.05; and ***P* value ≤ 0.01.

G and *H*) but not ablated (*SI Appendix*, Fig. S8 *I* and *J*) larvae treated with 1μM PLX3397 when compared with 0.004% DMSO controls (*SI Appendix*, Fig. S8 *K* and *L*). Despite this, we observed accumulation of pyknotic nuclei in PLX3397-treated larvae at 4 dpi (*SI Appendix*, Fig. S8*J′*) suggesting that, consistent with published reports, PLX3397 alters macrophage function but not density (58, 59). Thus, we utilized PLX3397 treatment and *irf8* mutants to evaluate the requirement for MΦ/μglia during RPE regeneration.

To assess proliferation after RPE ablation, larvae were incubated in 10 mM BrdU from 3 to 4 dpi, the time of peak proliferation (18), and fixed immediately thereafter. At 4 dpi, *irf8* mutants unexpectedly showed significantly more BrdU$^+$ cells in the RPE when compared with wild-type siblings (Fig. 6 *A*–*C*). There was no significant difference in BrdU incorporation between unablated *irf8* wild-type and mutant controls (Fig. 6*C*), indicating that retention of proliferating cells was a result of MTZ-dependent RPE ablation and not the *irf8* mutation itself. A similar trend was seen in

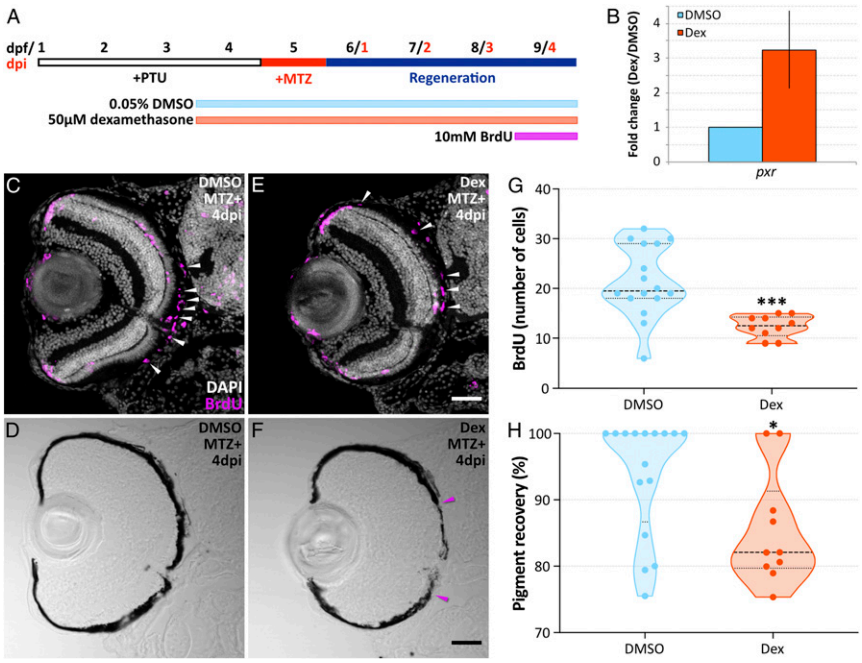

Fig. 5. Suppression of inflammation with dexamethasone impairs RPE regeneration. (*A*) Schematic depicting treatment timeline. (*B*) Bar graph showing fold change in *pxr* gene expression from larvae treated with dexamethasone or DMSO for 24 h (4 to 5 dpf). Error bar represents 95% CI. (*C–F*) Confocal micrographs of transverse sections from 4 dpi MTZ+ DMSO- (*C* and *D*) and dexamethasone-treated (*E* and *F*) Tg(*rpe65a*:nfsB-eGFP) eyes. (*C* and *E*) White arrowheads highlight BrdU$^+$ cells (magenta) in the RPE layer. White (DAPI) labels nuclei. (*F*) Magenta arrowheads designate edges of the regenerating RPE monolayer. (Scale bars, 40 μm.) (*G* and *H*) Violin plots showing a significant decrease in the number of BrdU$^+$ cells in the RPE (*G*) and the percent recovery of a pigmented monolayer (*H*) in MTZ+ dexamethasone-treated larvae. Dashed black lines represent the median, and dotted black lines represent quartiles. Statistical information can be found in *SI Appendix*, Table S12. Dorsal is up; *P value ≤ 0.05; and ***P value ≤ 0.001. PTU = n-phenylthiourea.

ablated PLX3397-treated larvae, which showed an increase in BrdU$^+$ cells in the RPE layer, though this did not achieve significance (Fig. 7 *A–C*). While increased proliferation was unanticipated based on dexamethasone treatment results (Fig. 5*G*), we also noted substantial accumulation of pyknotic nuclei between the photoreceptor layer and the RPE only in ablated *irf8* mutant (Fig. 6 *B* and *B'*) and PLX3397-treated (*SI Appendix*, Fig. S8*J'*) larvae.

To quantify the number of cells undergoing programmed cell death, we utilized terminal deoxynucleotidyl transferase dUTP nick end labeling (TUNEL). At 4 dpi, TUNEL$^+$ puncta accumulated between the outer plexiform layer and the basal RPE in *irf8* mutants (Fig. 6 *E* and *G*) and in PLX3397-treated larvae (Fig. 7*E*) when compared with sibling controls (Figs. 6 *D* and *F* and 7*D*). In *irf8* mutants, there was a range of TUNEL$^+$ staining and representative sections (Fig. 6 *D* and *E*) shown alongside extreme cases of TUNEL accumulation (Fig. 6 *F* and *G*); these specific datapoints are labeled in Fig. 6*H*. Quantification of the total number of TUNEL$^+$ puncta revealed no significant difference between unablated *irf8* wild-type and mutant (Fig. 6*H*) or DMSO- and PLX3397-treated (Fig. 7*F*) siblings, signifying that retention of dying cells resulted from MTZ-dependent RPE ablation, not the mutation in *irf8* or PLX3397 treatment. There were significant increases in the number of TUNEL$^+$ puncta between ablated *irf8* mutant and wild-type siblings (Fig. 6*H*) and between ablated DMSO- and PLX3397-treated siblings (Fig. 7*F*), indicating that dying cells are specifically retained in the damaged RPE of these larvae, supporting a role for MΦs/μglia in their removal. To confirm that the extent of RPE ablation did not differ as a result of the *irf8* mutation, PLX3397 or dexamethasone treatments, TUNEL$^+$ puncta were quantified at 6 dpf/1 dpi in each condition. Kruskal–Wallis tests revealed no significant variability among ablated larvae ($H = 10.39$, $P = 0.0649$), indicating that the magnitude of MTZ ablation is not affected by pharmacological treatment or genetic background (*SI Appendix*, Fig. S10 and Table S12).

To quantify RPE regeneration, we utilized recovery of *rpe65a*:nfsB-eGFP expression as a marker of RPE (18). RPE-ablated *irf8* wild-type and DMSO-treated larvae displayed more centralized recovery of continuous endogenous eGFP when compared with RPE-ablated *irf8* mutant or PLX3397-treated siblings (Figs. 6 *I* and *J* and 7 *G* and *H*). Overlaying eGFP onto brightfield images showed loss of RPE tissue integrity in the central injury site, which appeared larger in *irf8* mutant and PLX3397 treatment groups (Figs. 6 *K* and *L* and 7 *I* and *J*). To quantify RPE regeneration, dorsal and ventral angle measurements were made based on the edges of continuous eGFP expression in each larva (Fig. 6*M*). Results showed that RPE regeneration was significantly decreased in ablated *irf8* mutants (Fig. 6*N*) and PLX3397-treated larvae (Fig. 7*K*) when compared with sibling controls. Collectively, these results indicate that MΦ/μglia function is required for the timely progression of RPE regeneration.

Discussion

Harnessing the intrinsic ability of the RPE to self-repair is an attractive therapeutic approach to mitigating RPE degenerative diseases. Little is known about the signals driving RPE regeneration due to the difficulty of studying RPE repair in mammals, which have limited regenerative capacity. Recent characterization of a zebrafish RPE injury model has enabled us to begin to understand the molecular pathways regulating intrinsic RPE regeneration (18), and here we provide strong evidence that the immune response is involved. Specifically, we found that immune-related genes are up-regulated in regenerating RPE, that MΦs/μglia are the responsive leukocyte after RPE injury, and that MΦ/μglia function is required for RPE regeneration.

Our initial approach was to perform RNA-seq on FACS-isolated RPE to get a global picture of gene expression profiles after tissue damage. Of immediate interest was the up-regulation of known recruitment factors for neutrophils (*cxcl8* and *cxcl18*) and macrophages (*il34*) in RPE at early- and peak-regenerative time points (2 to 4 dpi). While robust neutrophil recruitment was not observed, MΦ/μglia infiltration was significant from 2 to 4 dpi concurrent with a significant up-regulation of cell cycle–related genes and MΦ/μglia proliferation. IL-34 is a ligand for CSF-1R and has been shown to promote proliferation and differentiation in macrophages and microglia (37), making it plausible that damaged RPE express *il34* to recruit MΦs/μglia for tissue repair. Indeed, we showed that treatment with PLX3397, a CSF-1R inhibitor shown to alter macrophage polarization (58, 59), impaired RPE regeneration. Further supporting this, O'Koren et al. found that IL-34–dependent microglia localized to and protected the integrity of the RPE and the BRB after photoreceptor damage in

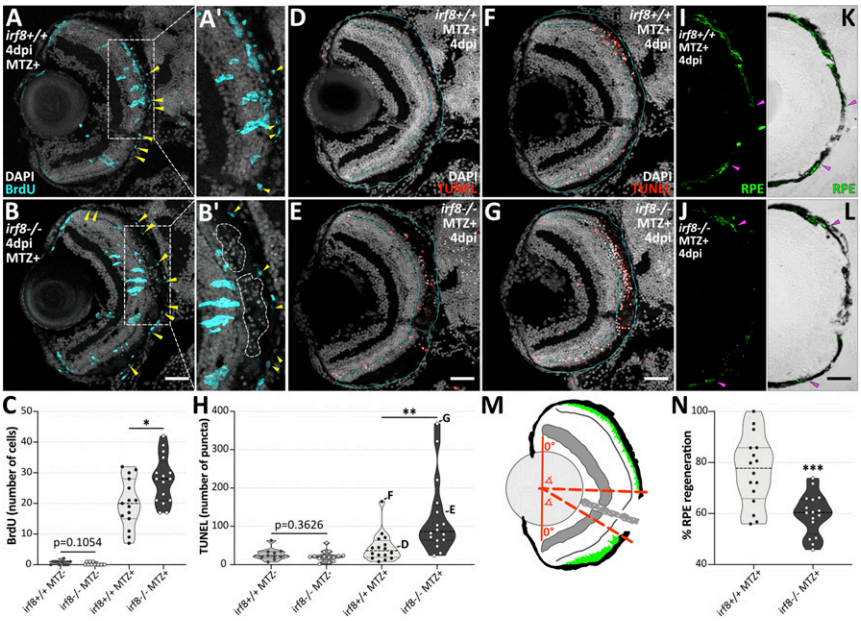

Fig. 6. *irf8* mutant larvae show impaired RPE regeneration. (*A* and *B*′) Confocal micrographs of transverse sections from 4 dpi MTZ+ *irf8*$^{+/+}$ (wild-type; *A*) and *irf8*$^{-/-}$ (mutant; *B*) eyes. Digital zooms highlight clusters of pyknotic nuclei retained between the outer plexiform layer and basal RPE in *irf8* mutants (*B*; white dashed lines). Yellow arrowheads mark BrdU^{+} cells (cyan) within the RPE layer. (*C*) Violin plots showing a significant increase in proliferative cells in the RPE of 4 dpi MTZ+ *irf8* mutants when compared with MTZ+ wild-type siblings. (*D*–*G*) Confocal micrographs showing TUNEL staining (red) on transverse sections from 4 dpi MTZ+ *irf8* wild-type (*D* and *F*) and *irf8* mutant (*E* and *G*) eyes. Images depict representative larvae (*D* and *E*) alongside larvae with the most TUNEL^{+} puncta (*F* and *G*). (*H*) Violin plots showing a significant increase in TUNEL labeling in 4 dpi MTZ+ *irf8* mutants when compared with 4 dpi MTZ+ wild-type siblings. (*C* and *H*) There was no significant difference between 9 dpf MTZ− *irf8* wild-type and mutant siblings. (*I*–*L*) Confocal micrographs of representative larvae (*D* and *E*) showing endogenous eGFP expression (*I* and *J*; green) and pigmentation relative to eGFP expansion (*K* and *L*). Magenta arrowheads delineate where continuous peripheral-to-central eGFP expression ends. (*M*) Schematic showing method of quantifying RPE regeneration. (*N*) Violin plots showing a significant decrease in RPE regeneration in 4 dpi MTZ+ *irf8* mutants. In all violin plots, dashed black lines represent the median, and dotted black lines represent quartiles. (Scale bars, 40 μm.) *SI Appendix*, Table S12 contains statistical information. Dorsal is up; **P* value ≤ 0.05; ***P* value ≤ 0.01; and ****P* value ≤ 0.001.

mice (27). Photoreceptors and RPE exist as a functional unit, and damage to one can elicit an injury response in the other (1). While O'Koren et al. did not determine if RPE was a source of IL-34 after photoreceptor damage, that IL-34–dependent microglia home to RPE under stress suggests this is a possibility in mammals (27).

il11b was the most significantly up-regulated DEG in RPE at 2 dpi. Interleukin 11 (IL-11) is induced by inflammation and functions as an anti-inflammatory cytokine and a survival and differentiation factor in the CNS (60). In the zebrafish retina, *il11a* and *il11b*, and their receptor, *gp130*, are expressed in Müller glia-derived progenitor cells (MGPCs) (61). Recombinant mammalian IL-11 promoted a modest increase in MGPC proliferation and reprogramming in the absence of retinal injury, which was more effective in combination with active leptin signaling (61). Interestingly, our RPE RNA-seq results showed that leptin (*lepb*) is up-regulated alongside *il11b* at 2 dpi (*SI Appendix*, Table S1). While the source of newly regenerated RPE in our model remains unknown, previous characterization has pointed to residual peripheral RPE that respond by proliferating after injury (18). Evidence for an RPE stem cell exists from studies in medaka (62) and in adult human donor RPE, where some cells could be induced to proliferate in vitro (16), but whether the zebrafish proliferating peripheral RPE are stem cell–like is not yet known. Nevertheless, expression of *il11b* and *lepb* by early-stage regenerating RPE is compelling and requires further examination.

Innate leukocytes predominate in zebrafish at larval ages. Tissue resident macrophages typically precede neutrophils at the injury site and are followed by recruited macrophages (63). Neutrophils play an important role in pathogen containment and mitigating infection, while macrophages are critical for tissue repair (63). Here, we showed no appreciable neutrophil accumulation upon MTZ ablation at any time points queried, though these cells were capable of infiltrating the eye after needle injury. Instead, MΦs/μglia dominated in the RPE after ablation. These results align with regenerative studies in the retina employing targeted genetic ablation (29, 64) or cytotoxic insult (30), while regenerative studies using ocular needle poke (29), and in nonocular tissues utilizing other approaches (e.g., tissue resection or cryoinjury), have showed robust infiltration of neutrophils followed by macrophage influx (19–21, 65, 66). The range in leukocyte responses to damage across injury paradigms may be based on the extent of the injury, the type of tissue, and/or the location within the organism, and risk of pathogen exposure. Indeed, studies where the injury site is exposed to the external environment reported robust neutrophil infiltration (21, 65, 66). Interestingly, impeding neutrophil infiltration had little effect on tissue regeneration (21, 65), indicating these cells may not be directly involved in tissue repair, consistent with our observation that neutrophils do not readily accumulate in the RPE after ablation.

In addition to increased infiltration after RPE ablation, we also qualitatively observed distinct morphology changes in 4C4^{+} MΦs/μglia that are often related to functional roles, such as phagocytosis (45). Specifically, we observed amoeboid phenotypes in 4C4^{+} cells from 2 to 4 dpi, while unablated controls showed more ramified morphologies and significantly fewer MΦs/μglia localized to the RPE. This observation aligns with previous findings that microglia become rounded and phagocytic in response to damage in zebrafish (25, 26, 29–31, 64) and mammalian (67) CNS tissues. Furthermore, our RNA-seq results indicate that, after RPE ablation, MΦs/μglia express phagocytosis markers [e.g., *anxa1a* (50, 51)] and cell cycle–related genes, consistent with other zebrafish studies (26, 31). In vivo, we observed that MΦs/μglia colocalized with RPE cell debris and actively proliferated in the retina and RPE after ablation. Quantitatively, we detected a significant increase in the sphericity of anterior MΦs/μglia during peak infiltration at 3 dpi. We chose to measure sphericity in the entire population of anterior MΦs/μglia as previous studies have reported reactivity of phagocytic cells outside the immediate injury site (29, 64); thus, it is possible that more localized sphericity differences exist at 2 and 4 dpi.

Several phases have been characterized following tissue injury: 1) the inflammatory phase, when leukocytes are recruited, secrete proinflammatory cytokines, and begin phagocytosis; 2) the resolution phase, when macrophages continue to phagocytose cell debris and shift from pro- to anti-inflammatory phenotypes; and 3) the regeneration phase, when injured tissues initiate proliferation (65, 68). Indeed, sequential progression of resolution and regeneration phases have been shown after tail-fin resection in

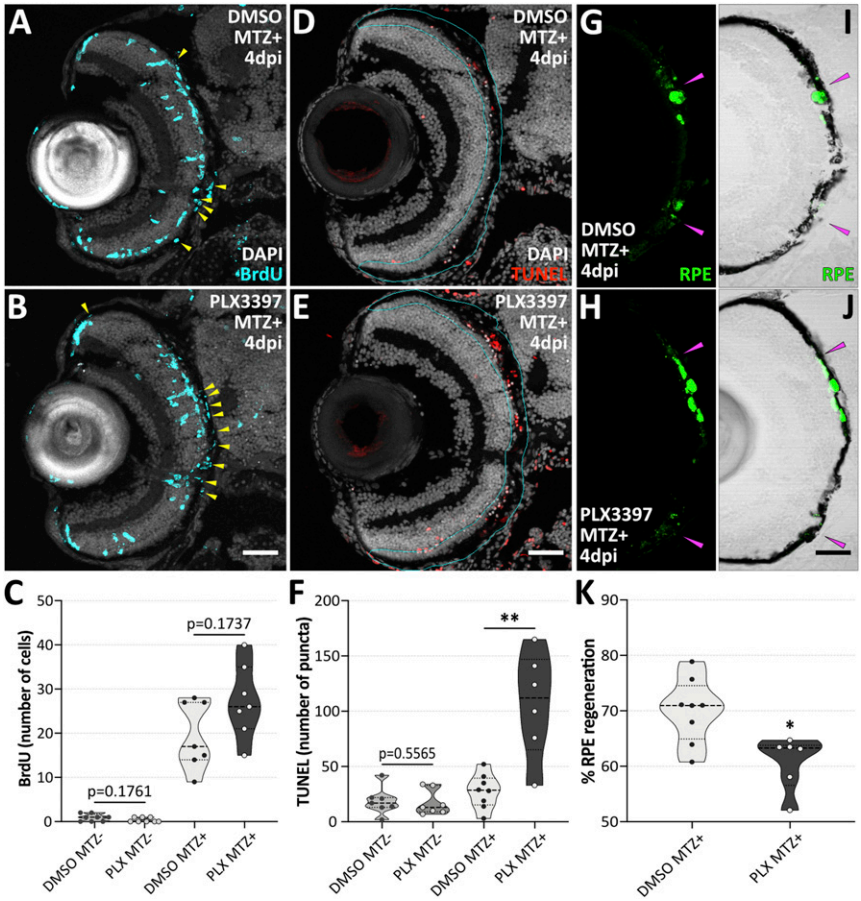

Fig. 7. Treatment with the CSF-1R inhibitor, PLX3397, impairs RPE regeneration. Confocal micrographs of transverse sections showing BrdU (*A* and *B*; cyan) and TUNEL (*D* and *E*; red) staining and endogenous eGFP (*G–J*; green) from 4 dpi MTZ+ DMSO- and PLX3397-treated larvae. White (DAPI) labels nuclei. Violin plots showing quantification of BrdU (*C*) and TUNEL (*F*) in 9 dpf MTZ– and 4 dpi MTZ+ larval treatment groups. (*C*) Although not significant, the number of $BrdU^+$ cells in the RPE (*A* and *B*; yellow arrowheads) trends upward in 4 dpi MTZ+ PLX3397-treated larvae when compared with 4 dpi MTZ+ DMSO controls. (*F*) A significant increase was observed in the number of $TUNEL^+$ puncta between the outer plexiform layer and basal RPE (*D* and *E*; cyan line) of 4 dpi MTZ+ PLX3397-treated larvae when compared with 4 dpi MTZ+ DMSO controls. In *G* and *H*, magenta arrowheads delineate where continuous peripheral-to-central eGFP expression ends, and brightfield confocal micrographs show pigmentation relative to eGFP expansion (*I* and *J*; magenta arrowheads). (*K*) Violin plots showing a significant decrease in RPE regeneration in 4 dpi MTZ+ PLX3397-treated larvae. (Scale bars, 40 μm.) In all violin plots, dashed black lines represent the median, and dotted black lines represent quartiles. *SI Appendix*, Table S12 contains statistical information. Dorsal is up; **P* value ≤ 0.05; and ***P* value ≤ 0.01.

zebrafish (65). We propose that similar phases exist during RPE regeneration (Fig. 8). Our previous characterization of RPE regeneration showed that proliferation peaked in the RPE and pigmentation recovered between 3 to 4 dpi (18). Here, we show that MΦ/μglia infiltration into the RPE injury site occurs between 1 to 2 dpi, peaks at 3 dpi, and wanes by 4 dpi, representing a potential window when inflammation is resolved (Fig. 8; 2 to 4 dpi). Building off of these data, it appears that functional (e.g., phagocytic) MΦ/μglia presence in the injury site precedes as well as overlaps with peak RPE proliferation and visible recovery of pigmentation; thus, 3 to 4 dpi may represent a critical window after RPE ablation when the resolution phase ends and regeneration begins (Fig. 8).

In agreement with previous reports in multiple reparative contexts (19, 21, 24, 29, 32, 65), we demonstrate that inflammation and MΦs/μglia activity contribute to RPE regeneration in vivo. Synthetic GCs have been widely used to suppress inflammation by attenuating the inflammatory phase after injury and driving macrophages toward an anti-inflammatory phenotype (68, 69). Results here support the existence of an inflammatory phase during RPE regeneration, as evidenced by expression of phagocytic (e.g., *anxa1a*) and proinflammatory genes (e.g., *cxcl8a* and *cxcl18b*) and recruitment of MΦs/μglia to the ablated RPE (Fig. 8). Inhibition of inflammation using dexamethasone resulted in decreased proliferation in the RPE layer and delayed recovery of a pigmented monolayer. These findings align with studies in the zebrafish retina, which showed less proliferative MGPCs and reduced photoreceptor regeneration after dexamethasone treatment (29, 32).

Using both an *irf8* mutant and PLX3397, we showed that RPE regeneration is impaired after ablation. Retention of pyknotic nuclei and $TUNEL^+$ debris in and adjacent to the RPE injury site was a prominent phenotype in RPE-ablated *irf8* mutants and PLX3397-treated larvae. While MΦs/μglia were present in the injury site of *irf8* mutant and PLX3397-treated larvae, *irf8* mutants possessed smaller $4C4^+$ cells, suggesting that these cells may be immature (33) and thus ill-equipped to remove debris. For PLX3397, previous studies have shown CSF-1R inhibition induced defects in macrophage polarization to an anti-inflammatory phenotype in tumors, effectively altering the tissue microenvironment without cell depletion (58, 59). Pro- and anti-inflammatory phenotypes have been characterized in zebrafish macrophages (70) and thus it is plausible that altered MΦ/μglia polarization impacts RPE regeneration in PLX3397-treated larvae regardless of infiltration. While MΦ/μglia infiltration was also unaffected in dexamethasone-treated larvae, pyknotic nuclei did not accumulate, indicating intact phagocytic function. Despite this, the outcome was still impaired RPE regeneration. GCs have been shown to have varying effects on macrophage migration (69); indeed, in GC-treated zebrafish after wounding, leukocyte migration defects were detected in some injury paradigms (19, 29, 32) but not others (71, 72). Furthermore, GCs have been shown to increase phagocytosis by macrophages to promote expedited resolution of inflammation (68, 69), which may explain the lack of pyknotic nuclei accumulation in dexamethasone-treated larvae after RPE damage. Collectively, the results from dexamethasone, *irf8* mutant, and PLX3397 treatment experiments hint at the existence of critical inflammatory and resolution phases after RPE ablation, and we provide evidence that bypassing either results in the same outcome: impairment of RPE regeneration. Importantly, retention of MΦ/μglia populations, despite these perturbations, provides a unique system in which to further study how these cellular functions (e.g., phagocytosis, polarization, etc.) contribute to RPE regeneration.

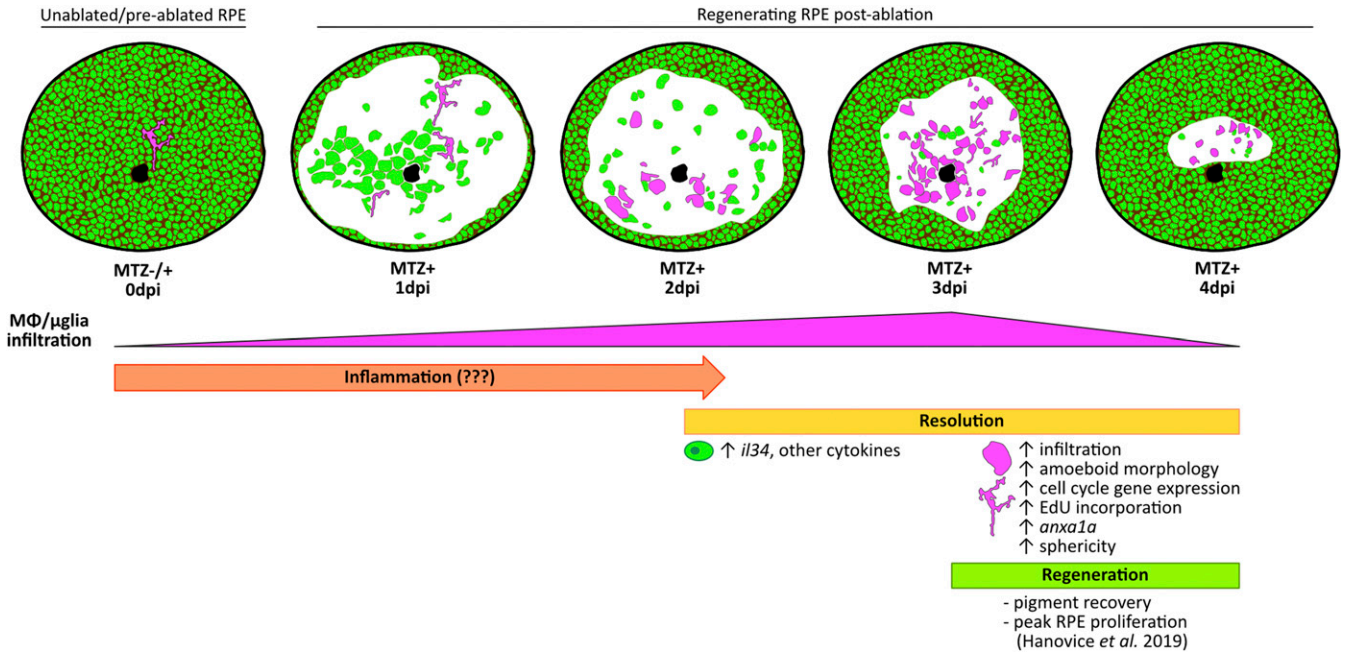

Fig. 8. Phases of immune involvement during RPE regeneration. Schematic showing few ramified MΦs/μglia (magenta) present in the RPE (green) of unablated larvae. Infiltration of MΦs/μglia to the central RPE injury site after ablation begins at 2 dpi, peaks at 3 dpi, and wanes by 4 dpi, representing a time window when inflammation is likely resolved (2 to 4 dpi; yellow). During resolution, MΦs/μglia appear amoeboid in morphology, proliferate and express phagocytosis markers (e.g., *anxa1a*), and RPE express *il34* and other cytokines. Peak RPE layer proliferation and recovery of pigment occurs between 3 to 4 dpi (18). This coupled with the decreased presence of MΦs/μglia in the RPE by 4 dpi may hint to a time window after ablation (3 to 4 dpi; green) when inflammation has been resolved, enabling peak RPE regeneration.

Lastly and paradoxically, we observed an increase in proliferating cells in the RPE of *irf8* mutants and a trending increase in PLX3397-treated larvae after ablation. While increased proliferation may seem beneficial in the context of regeneration, RPE overproliferation can lead to pathology, as in proliferative vitreoretinopathy (13). We have shown that proliferation tapers off in the RPE at 4 to 5 dpi (18), so prolonged proliferation is likely not advantageous for RPE regeneration. In support of this, despite the presence of more $BrdU^+$ cells, RPE regeneration is impaired in both *irf8* mutants and PLX3397-treated larvae. A possible explanation for the increase in proliferation is the lingering $TUNEL^+$ cells, as signaling via apoptotic bodies has been shown to induce proliferation in different injury contexts (73, 74). The emergence of apoptotic and proliferating cells coincide within the first 24 h after RPE injury (18), suggesting that apoptosis could be an additional factor driving proliferation.

Materials and Methods

Additional details are located in *SI Appendix, Materials and Methods*.

Zebrafish Maintenance and Husbandry. Zebrafish (*SI Appendix*, Table S11) were handled in compliance with University of Pittsburgh Institutional Animal Care and Use Committee regulations. Adult zebrafish were housed at 28.5 °C on a 14-/10-h light/dark cycle. Embryos were housed in a 28.5 °C incubator (no light/dark cycle) until euthanasia by tricaine (MS-222; Fisher Scientific) overdose. Larvae euthanized on or before 9 dpf were unfed (75), while those aged past 9 dpf were fed Zeigler AP100 size 2 (Zeigler Bros, Inc).

MTZ, Dexamethasone, and PLX3397 Treatment. RPE ablation by MTZ was performed after (18). The timing of dexamethasone and PLX3397 treatments closely follow White et al. (29), with modification. Larvae were treated with 50 μM dexamethasone (Sigma-Aldrich), 1 μM PLX3397 (Selleck Chemicals), or 0.05% or 0.004% DMSO (vehicle controls) for 24 h prior to RPE ablation, for the duration of MTZ treatment, until fixation.

Needle Injury. At 5 dpf, larvae were tricaine anesthetized, immobilized in 0.5% low melt agarose, and a flame-sharpened tungsten needle was used to puncture the ventral retina. Larvae recovered in system water for 12 h and were fixed for analysis.

Tissue Dissociation and FACS. Euthanized larvae were transferred to ice-cold 1× PBS for bilateral enucleations; eyes were subsequently pooled. Tissue dissociation procedures were modified from refs. 76 and 77 and utilized sequential enzymatic digestion with collagenase, then trypsin (RPE sorts), or trypsin then mechanical needle dissociation (MΦ/μglia sorts). Prior to FACS, all samples underwent straining, washing, and labeling with LIVE/DEAD Fixable Aqua Dead Cell Stain (1:1,000; Invitrogen). Sorting gates were set using unstained and single-channel controls, when appropriate, and gated cells were sorted directly into complementary DNA (cDNA) preparation reagents. All sorting was performed by the Flow Cytometry Core at the University of Pittsburgh School of Medicine Department of Pediatrics using a FACSAria IIu cell sorter (BD Biosciences).

RNA-Seq and Bioinformatics. cDNA and library preparation, quality control analyses, and sequencing was performed by the Health Sciences Sequencing Core at Children's Hospital of Pittsburgh using established protocols and following manufacturer instructions. Aiming for 40 million reads/sample, 75 cycle, 2 × 75 bp paired-end sequencing was performed on a NextSeq 500 system (Illumina, Inc.). Raw read data were imported into CLC Genomics Workbench (Qiagen Digital Insights) licensed through the Molecular Biology Information Service of the Health Sciences Library System at the University of Pittsburgh. Read quality assessment was based on Phred-scores (78), and sample variation was evaluated using principal component analysis (PCA; *SI Appendix*, Figs. S5*E* and S11). CLC Genomics Workbench was used for read processing, mapping, differential expression analyses, PCA plot, and heatmap generation. Pathway enrichment analyses were performed on filtered DEGs using the PANTHER statistical overrepresentation test (www.pantherdb.org/; released April 7, 2020).

Genotyping PCR and qRT-PCR. Animals from $irf8^{st95}$ crosses were genotyped as described (*SI Appendix*, Table S11; ref. 33). For qRT-PCR, total RNA was purified from homogenized tissue using the RNeasy Plus Mini Kit (Qiagen), and cDNA was synthesized using the iScript cDNA Synthesis Kit (Bio-Rad Laboratories) or prepped from FACS-isolated RPE. Reactions were run on a CFX384 Touch Real-Time PCR Detection System using iTaq Universal SYBR Green Supermix (both Bio-Rad Laboratories) and primers amplifying *irf8*, *rpe65a*, *pxr*, and *actb1*

(reference gene; *SI Appendix*, Table S11). Fold change and relative expression were calculated using the comparative C_T method (79).

Immunohistochemistry. Euthanized larvae were fixed in 4% paraformaldehyde for 2 to 3 h at room temperature or at 4 °C overnight. Staining was performed as described (18) using established protocols for sectioned (80) or whole-mount tissue (81), with modification.

BrdU/EdU Incorporation and TUNEL Assays. Larvae were exposed to 10 mM BrdU (Sigma-Aldrich) in system water for 24 h prior to fixation. EdU incorporation was performed using the Click-iT EdU Cell Proliferation Kit (Invitrogen), and larvae were treated in system water for 2 h prior to fixation. TUNEL assays were performed using the TMR red In Situ Cell Death Detection Kit (Roche) or the Click-iT Plus TUNEL Assay for In Situ Apoptosis Detection kit (Invitrogen) following manufacturer protocols.

Imaging Data Acquisition, Processing, and Quantification. *Confocal microscopy.* Images were acquired using an Olympus Fluoview FV1200 laser scanning microscope (Olympus Corporation). Sectioned tissue was imaged using a 40× (1.30 NA) oil immersion lens, and whole-mount tissue was imaged using a 20× (0.85 NA) oil immersion lens (both Olympus Corporation). Raw imaging data were quantified and processed for presentation in figures and movies using FIJI (ImageJ; ref. 82) or Imaris version 9.6 (Bitplane). Cell and puncta count quantification was done manually using the Cell Counter plug-in or automated using the Analyze Particles function in FIJI. Percent area quantification was performed on 8-bit maximum-projected z-stacks in FIJI, and regions of interest were generated manually using the polygon selection tool. Percent pigment recovery and RPE regeneration were quantified in FIJI by making dorsal and ventral angle measurements utilizing a reference line with midpoint (see schematics in Fig. 6*M* and *SI Appendix*, Fig. S6*A*).

In vivo light-sheet microscopy. Experiments used embryos collected from *rpe65a:*nfsB-eGFP × *mpeg1.1:*Dendra2 outcrosses. Data were acquired using the Tilt light-sheet imaging system (Mizar Imaging; ref. 83), a 20× (0.95 NA) water immersion lens, and NIS-Elements software (both Nikon Corporation). Immediately prior to image acquisition, Dendra2 (green) was photoconverted to Dendra2 (red) by 1-min exposure to an Intensilight C-HGFI (Nikon Corporation) UV laser. 3D deconvolution was performed in NIS-Elements, and deconvolved z-stack files were 3D rendered for sphericity quantification using Imaris.

Statistical Analysis. Statistical analyses and graphical representation of raw data were performed using Prism 8/9 (GraphPad Software). Normal (Gaussian) distribution was assessed using the D'Agostino–Pearson omnibus normality test. In datasets with a normal distribution, significance was determined using the unpaired *t* test with Welch's correction; in datasets with nonnormal distribution or $n < 8$, nonparametric Mann–Whitney *U* tests were performed to calculate *P* values. Kruskal–Wallis one-way ANOVA with Dunn's post hoc test was used to determine variance and perform multiple comparisons, respectively. For graphs, the median represents the measure of center unless otherwise stated. *SI Appendix*, Table S12 contains detailed statistical information.

Data Availability. Raw and processed RNA-seq data have been deposited in the National Center for Biotechnology Information Gene Expression Omnibus (NCBI GEO), accessible through GSE155294 (RPE dataset) and GSE155295 (MΦ/μglia dataset).

ACKNOWLEDGMENTS. This work was supported by the NIH (Grant T32-EY17271 [L.L.L.], Grant RO1-EY29410 [J.M.G.], and NIH Core Grant P30-EY08098 [Department of Ophthalmology]), the University of Pittsburgh Medical Center (UPMC) Immune Transplant and Therapy Center (L.L.L. and J.M.G.), the Pennsylvania Lions Sight Conservation and Eye Research Foundation (L.L.L. and J.M.G.), the Whitman Center at the Marine Biological Laboratory (J.M.G.), the Charles and Louella Snyder Retinal Regeneration Fund (J.M.G.), the BrightFocus Foundation Macular Degeneration Research Program (Grant M2016067 [J.M.G.]), the E. Ronald Salvitti Chair in Ophthalmology Research (J.M.G.), the Martha Wandrisco Neff Research Award in Macular Degeneration (L.L.L. and N.J.H.), a University of Pittsburgh Honors College Health Sciences Fellowship (S.M.G.), the Eye & Ear Foundation of Pittsburgh, and an unrestricted grant from Research to Prevent Blindness. We thank Dr. G. Burch Fisher III for statistical discussion and expertise, Veronica Spector for editorial assistance, Dr. Hugh Hammer for expert zebrafish care, Drs. Paul Maddox and Joel Smith for advice on light-sheet microscopy, and Dr. Marko Horb and his laboratory for hosting J.M.G. and L.L.L. at the Marine Biological Laboratory.

1. O. Strauss, The retinal pigment epithelium in visual function. *Physiol. Rev.* **85**, 845–881 (2005).
2. P. Tanna, R. W. Strauss, K. Fujinami, M. Michaelides, Stargardt disease: Clinical features, molecular genetics, animal models and therapeutic options. *Br. J. Ophthalmol.* **101**, 25–30 (2017).
3. D. T. Hartong, E. L. Berson, T. P. Dryja, Retinitis pigmentosa. *Lancet* **368**, 1795–1809 (2006).
4. J. P. Sarks, S. H. Sarks, M. C. Killingsworth, Evolution of geographic atrophy of the retinal pigment epithelium. *Eye (Lond.)* **2**, 552–577 (1988).
5. D. S. McLeod *et al.*, Relationship between RPE and choriocapillaris in age-related macular degeneration. *Invest. Ophthalmol. Vis. Sci.* **50**, 4982–4991 (2009).
6. S. R. Flaxman *et al.*; Vision Loss Expert Group of the Global Burden of Disease Study, Global causes of blindness and distance vision impairment 1990-2020: A systematic review and meta-analysis. *Lancet Glob. Health* **5**, e1221–e1234 (2017).
7. N. G. Ghazi *et al.*, Treatment of retinitis pigmentosa due to MERTK mutations by ocular subretinal injection of adeno-associated virus gene vector: Results of a phase I trial. *Hum. Genet.* **135**, 327–343 (2016).
8. M. S. Mehat *et al.*, Transplantation of human embryonic stem cell-derived retinal pigment epithelial cells in macular degeneration. *Ophthalmology* **125**, 1765–1775 (2018).
9. M. Zarbin, I. Sugino, E. Townes-Anderson, Concise review: Update on retinal pigment epithelium transplantation for age-related macular degeneration. *Stem Cells Transl. Med.* **8**, 466–477 (2019).
10. D. Ail, M. Perron, Retinal degeneration and regeneration-lessons from fishes and amphibians. *Curr. Pathobiol. Rep.* **5**, 67–78 (2017).
11. D. Goldman, Müller glial cell reprogramming and retina regeneration. *Nat. Rev. Neurosci.* **15**, 431–442 (2014).
12. M. S. Wilken, T. A. Reh, Retinal regeneration in birds and mice. *Curr. Opin. Genet. Dev.* **40**, 57–64 (2016).
13. I. Grierson *et al.*, Development, repair and regeneration of the retinal pigment epithelium. *Eye (Lond.)* **8**, 255–262 (1994).
14. H. Xia, M. P. Krebs, S. Kaushal, E. W. Scott, Enhanced retinal pigment epithelium regeneration after injury in MRL/MpJ mice. *Exp. Eye Res.* **93**, 862–872 (2011).
15. D. Kampik *et al.*, In situ regeneration of retinal pigment epithelium by gene transfer of E2F2: A potential strategy for treatment of macular degenerations. *Gene Ther.* **24**, 810–818 (2017).
16. E. Salero *et al.*, Adult human RPE can be activated into a multipotent stem cell that produces mesenchymal derivatives. *Cell Stem Cell* **10**, 88–95 (2012).
17. C. Chiba, The retinal pigment epithelium: An important player of retinal disorders and regeneration. *Exp. Eye Res.* **123**, 107–114 (2014).
18. N. J. Hanovice *et al.*, Regeneration of the zebrafish retinal pigment epithelium after widespread genetic ablation. *PLoS Genet.* **15**, e1007939 (2019).
19. T. M. Tsarouchas *et al.*, Dynamic control of proinflammatory cytokines Il-1β and Tnf-α by macrophages in zebrafish spinal cord regeneration. *Nat. Commun.* **9**, 4670 (2018).
20. S. Xu, S. E. Webb, T. C. K. Lau, S. H. Cheng, Matrix metalloproteinases (MMPs) mediate leukocyte recruitment during the inflammatory phase of zebrafish heart regeneration. *Sci. Rep.* **8**, 7199 (2018).
21. T. A. Petrie, N. S. Strand, C.-T. Yang, J. S. Rabinowitz, R. T. Moon, Macrophages modulate adult zebrafish tail fin regeneration. *Development* **142**, 406 (2015).
22. A. L. Mescher, Macrophages and fibroblasts during inflammation and tissue repair in models of organ regeneration. *Regeneration (Oxf.)* **4**, 39–53 (2017).
23. A. G. W. Sandoval, M. Maden, Regeneration in the spiny mouse, Acomys, a new mammalian model. *Curr. Opin. Genet. Dev.* **64**, 31–36 (2020).
24. N. Kyritsis *et al.*, Acute inflammation initiates the regenerative response in the adult zebrafish brain. *Science* **338**, 1353–1356 (2012).
25. C. Herzog *et al.*, Rapid clearance of cellular debris by microglia limits secondary neuronal cell death after brain injury in vivo. *Development* **146**, dev174698 (2019).
26. N. Oosterhof *et al.*, Identification of a conserved and acute neurodegeneration-specific microglial transcriptome in the zebrafish. *Glia* **65**, 138–149 (2017).
27. E. G. O'Koren *et al.*, Microglial function is distinct in different anatomical locations during retinal homeostasis and degeneration. *Immunity* **50**, 723–737.e7 (2019).
28. W. Ma *et al.*, Monocyte infiltration and proliferation reestablish myeloid cell homeostasis in the mouse retina following retinal pigment epithelial cell injury. *Sci. Rep.* **7**, 8433 (2017).
29. D. T. White *et al.*, Immunomodulation-accelerated neuronal regeneration following selective rod photoreceptor cell ablation in the zebrafish retina. *Proc. Natl. Acad. Sci. U.S.A.* **114**, E3719–E3728 (2017).
30. D. M. Mitchell, A. G. Lovel, D. L. Stenkamp, Dynamic changes in microglial and macrophage characteristics during degeneration and regeneration of the zebrafish retina. *J. Neuroinflammation* **15**, 163 (2018).
31. D. M. Mitchell, C. Sun, S. S. Hunter, D. D. New, D. L. Stenkamp, Regeneration associated transcriptional signature of retinal microglia and macrophages. *Sci. Rep.* **9**, 4768 (2019).
32. N. J. Silva *et al.*, Inflammation and matrix metalloproteinase 9 (Mmp-9) regulate photoreceptor regeneration in adult zebrafish. *Glia* **68**, 1445–1465 (2020).
33. C. E. Shiau, Z. Kaufman, A. M. Meireles, W. S. Talbot, Differential requirement for irf8 in formation of embryonic and adult macrophages in zebrafish. *PLoS One* **10**, e0117513 (2015).
34. C. P. Hamel *et al.*, Molecular cloning and expression of RPE65, a novel retinal pigment epithelium-specific microsomal protein that is post-transcriptionally regulated in vitro. *J. Biol. Chem.* **268**, 15751–15757 (1993).
35. S. Curado *et al.*, Conditional targeted cell ablation in zebrafish: A new tool for regeneration studies. *Dev. Dyn.* **236**, 1025–1035 (2007).

36. H. Lin *et al*., Discovery of a cytokine and its receptor by functional screening of the extracellular proteome. *Science* **320**, 807–811 (2008).
37. M. Baghdadi *et al*., Interleukin-34, a comprehensive review. *J. Leukoc. Biol.* **104**, 931–951 (2018).
38. C. Guillonneau, S. Bézie, I. Anegon, Immunoregulatory properties of the cytokine IL-34. *Cell. Mol. Life Sci.* **74**, 2569–2586 (2017).
39. S. de Oliveira *et al*., Cxcl8 (IL-8) mediates neutrophil recruitment and behavior in the zebrafish inflammatory response. *J. Immunol.* **190**, 4349–4359 (2013).
40. V. Torraca, N. A. Otto, A. Tavakoli-Tameh, A. H. Meijer, The inflammatory chemokine Cxcl18b exerts neutrophil-specific chemotaxis via the promiscuous chemokine receptor Cxcr2 in zebrafish. *Dev. Comp. Immunol.* **67**, 57–65 (2017).
41. N. S. Trede, D. M. Langenau, D. Traver, A. T. Look, L. I. Zon, The use of zebrafish to understand immunity. *Immunity* **20**, 367–379 (2004).
42. P. Y. Lam, S. K. Yoo, J. M. Green, A. Huttenlocher, The SH2-domain-containing inositol 5-phosphatase (SHIP) limits the motility of neutrophils and their recruitment to wounds in zebrafish. *J. Cell Sci.* **125**, 4973–4978 (2012).
43. S. E. L. Craig, A.-A. Calinescu, P. F. Hitchcock, Identification of the molecular signatures integral to regenerating photoreceptors in the retina of the zebra fish. *J. Ocul. Biol. Dis. Infor.* **1**, 73–84 (2008).
44. F. Ellett, L. Pase, J. W. Hayman, A. Andrianopoulos, G. J. Lieschke, mpeg1 promoter transgenes direct macrophage-lineage expression in zebrafish. *Blood* **117**, e49–e56 (2011).
45. F. R. Walker *et al*., Dynamic structural remodelling of microglia in health and disease: A review of the models, the signals and the mechanisms. *Brain Behav. Immun.* **37**, 1–14 (2014).
46. E. A. Harvie, J. M. Green, M. N. Neely, A. Huttenlocher, Innate immune response to *Streptococcus iniae* infection in zebrafish larvae. *Infect. Immun.* **81**, 110–121 (2013).
47. D. M. Chudakov, S. Lukyanov, K. A. Lukyanov, Tracking intracellular protein movements using photoswitchable fluorescent proteins PS-CFP2 and Dendra2. *Nat. Protoc.* **2**, 2024–2032 (2007).
48. H. Wadell, Volume, shape, and roundness of rock particles. *J. Geol.* **40**, 443–451 (1932).
49. M. H. Sieweke, J. E. Allen, Beyond stem cells: Self-renewal of differentiated macrophages. *Science* **342**, 1242974 (2013).
50. J. Dalli *et al*., Annexin A1 regulates neutrophil clearance by macrophages in the mouse bone marrow. *FASEB J.* **26**, 387–396 (2012).
51. S. Yona *et al*., Impaired phagocytic mechanism in annexin 1 null macrophages. *Br. J. Pharmacol.* **148**, 469–477 (2006).
52. T. A. Wynn, K. M. Vannella, Macrophages in tissue repair, regeneration, and fibrosis. *Immunity* **44**, 450–462 (2016).
53. D. Shi, D. Yang, B. Yan, Dexamethasone transcriptionally increases the expression of the pregnane X receptor and synergistically enhances pyrethroid esfenvalerate in the induction of cytochrome P450 3A23. *Biochem. Pharmacol.* **80**, 1274–1283 (2010).
54. T. Tamura, T. Nagamura-Inoue, Z. Shmeltzer, T. Kuwata, K. Ozato, ICSBP directs bipotential myeloid progenitor cells to differentiate into mature macrophages. *Immunity* **13**, 155–165 (2000).
55. K. Kierdorf *et al*., Microglia emerge from erythromyeloid precursors via Pu.1- and Irf8-dependent pathways. *Nat. Neurosci.* **16**, 273–280 (2013).
56. F. M. Conedera, A. M. Q. Pousa, N. Mercader, M. Tschopp, V. Enzmann, Retinal microglia signaling affects Müller cell behavior in the zebrafish following laser injury induction. *Glia* **67**, 1150–1166 (2019).
57. A. S. de Preux Charles, T. Bise, F. Baier, J. Marro, A. Jaźwińska, Distinct effects of inflammation on preconditioning and regeneration of the adult zebrafish heart. *Open Biol.* **6**, 160102 (2016).
58. D. G. DeNardo *et al*., Leukocyte complexity predicts breast cancer survival and functionally regulates response to chemotherapy. *Cancer Discov.* **1**, 54–67 (2011).
59. J. Y. Ao *et al*., Colony-stimulating factor 1 receptor blockade inhibits tumor growth by altering the polarization of tumor-associated macrophages in hepatocellular carcinoma. *Mol. Cancer Ther.* **16**, 1544–1554 (2017).
60. D. H. Xu *et al*., The role of IL-11 in immunity and cancer. *Cancer Lett.* **373**, 156–163 (2016).
61. X. F. Zhao *et al*., Leptin and IL-6 family cytokines synergize to stimulate Müller glia reprogramming and retina regeneration. *Cell Rep.* **9**, 272–284 (2014).
62. R. Reinhardt *et al*., Sox2, Tlx, Gli3, and Her9 converge on Rx2 to define retinal stem cells in vivo. *EMBO J.* **34**, 1572–1588 (2015).
63. M. C. Keightley, C. H. Wang, V. Pazhakh, G. J. Lieschke, Delineating the roles of neutrophils and macrophages in zebrafish regeneration models. *Int. J. Biochem. Cell Biol.* **56**, 92–106 (2014).
64. T. J. van Ham *et al*., Intravital correlated microscopy reveals differential macrophage and microglial dynamics during resolution of neuroinflammation. *Dis. Model. Mech.* **7**, 857–869 (2014).
65. L. Li, B. Yan, Y. Q. Shi, W. Q. Zhang, Z. L. Wen, Live imaging reveals differing roles of macrophages and neutrophils during zebrafish tail fin regeneration. *J. Biol. Chem.* **287**, 25353–25360 (2012).
66. C. A. Loynes *et al*., PGE_2 production at sites of tissue injury promotes an anti-inflammatory neutrophil phenotype and determines the outcome of inflammation resolution in vivo. *Sci. Adv.* **4**, eaar8320 (2018).
67. C. Zhang, T. T. Lam, M. O. Tso, Heterogeneous populations of microglia/macrophages in the retina and their activation after retinal ischemia and reperfusion injury. *Exp. Eye Res.* **81**, 700–709 (2005).
68. T. Desgeorges, G. Caratti, R. Mounier, J. Tuckermann, B. Chazaud, Glucocorticoids shape macrophage phenotype for tissue repair. *Front. Immunol.* **10**, 1591 (2019).
69. J. M. Ehrchen, J. Roth, K. Barczyk-Kahlert, More than suppression: Glucocorticoid action on monocytes and macrophages. *Front. Immunol.* **10**, 2028 (2019).
70. M. Nguyen-Chi *et al*., Identification of polarized macrophage subsets in zebrafish. *eLife* **4**, e07288 (2015).
71. Y. Xie *et al*., Glucocorticoids inhibit macrophage differentiation towards a pro-inflammatory phenotype upon wounding without affecting their migration. *Dis. Model. Mech.* **12**, dmm037887 (2019).
72. A. Chatzopoulou *et al*., Glucocorticoid-induced attenuation of the inflammatory response in zebrafish. *Endocrinology* **157**, 2772–2784 (2016).
73. S. Chera *et al*., Apoptotic cells provide an unexpected source of Wnt3 signaling to drive hydra head regeneration. *Dev. Cell* **17**, 279–289 (2009).
74. C. K. Brock *et al*., Stem cell proliferation is induced by apoptotic bodies from dying cells during epithelial tissue maintenance. *Nat. Commun.* **10**, 1044 (2019).
75. R. E. Hernandez, L. Galitan, J. Cameron, N. Goodwin, L. Ramakrishnan, Delay of initial feeding of zebrafish larvae until 8 days postfertilization has no impact on survival or growth through the juvenile stage. *Zebrafish* **15**, 515–518 (2018).
76. R. A. Uribe, J. M. Gross, Id2a influences neuron and glia formation in the zebrafish retina by modulating retinoblast cell cycle kinetics. *Development* **138**, 179 (2011).
77. K. L. Sinagoga *et al*., Distinct roles for the mTOR pathway in postnatal morphogenesis, maturation and function of pancreatic islets. *Development* **144**, 2402–2414 (2017).
78. B. Ewing, L. Hillier, M. C. Wendl, P. Green, Base-calling of automated sequencer traces using phred. I. Accuracy assessment. *Genome Res.* **8**, 175–185 (1998).
79. K. J. Livak, T. D. Schmittgen, Analysis of relative gene expression data using real-time quantitative PCR and the 2(-Delta Delta C(T)) method. *Methods* **25**, 402–408 (2001).
80. R. A. Uribe, J. M. Gross, Immunohistochemistry on cryosections from embryonic and adult zebrafish eyes. *CSH Protoc* **2007**, prot4779 (2007).
81. L. Maves, W. Jackman, C. B. Kimmel, FGF3 and FGF8 mediate a rhombomere 4 signaling activity in the zebrafish hindbrain. *Development* **129**, 3825–3837 (2002).
82. J. Schindelin *et al*., Fiji: An open-source platform for biological-image analysis. *Nat. Methods* **9**, 676–682 (2012).
83. T. C. Fadero *et al*., LITE microscopy: Tilted light-sheet excitation of model organisms offers high resolution and low photobleaching. *J. Cell Biol.* **217**, 1869–1882 (2018).